

Edge Enriched 2D MoS₂ Thin Films Grown by Chemical Vapor Deposition for Enhanced Catalytic Performance

Sha Li,¹ Shanshan Wang,¹ Matteo M. Salamone,¹ Alex W. Robertson,¹ Simantini Nayak,² Heeyeon Kim,³ SC Edman Tsang,² Mauro Pasta,¹ Jamie H. Warner^{1}*

¹Department of Materials, University of Oxford, Parks Road, Oxford, OX1 3PH, UK

²Department of Chemistry, University of Oxford, South Parks Road, Oxford, OX1 3QR, UK

³Convergence Materials Laboratory, Korean Institute of Energy Research, 152 Gajeong-ro, Yuseong-gu, Daejeon 305-343, Korea

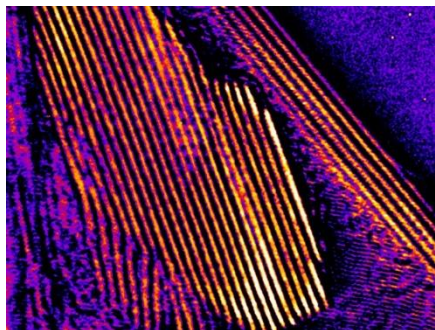
*Email: jamie.warner@materials.ox.ac.uk

Keywords: Porous thin film, Vertical platelet, Edge enriched MoS₂, Chemical vapor deposition (CVD), Hydrogen evolution reaction (HER), Catalyst

Abstract

Chemical vapor deposition (CVD) is used to grow thin films of 2D MoS₂ with nanostructure for catalytic applications in the hydrogen evolution reaction (HER). Tailoring of the CVD parameters results in an optimized MoS₂ structure for HER that consists of large MoS₂ platelets with smaller layered MoS₂ sheets growing off it in a perpendicular direction, which increases the total number of edge sites within a given geometric area. A surface area to geometric area ratio of up to ~ 340 is achieved, benefiting from the edge-exposed high porosity network structure. Optimized thickness of the MoS₂ film is determined for maximum performance, revealing that increasing thickness leads to increased impedance of the MoS₂ film and reduced current density. Current density of the optimum sample reaches as high as 60 mA/cm²_{geo} (normalized by geometric area) at an over-potential of 0.64 V vs. RHE (in 0.5 M H₂SO₄), with corresponding Tafel slope of ~ 90 mV/dec and exchange current density of 23 μA/cm²_{geo}. The lowered Tafel slope and large exchange current density demonstrate the high-porosity edge-exposed MoS₂ network structure is promising as a HER catalyst.

TOC graphics



Developing clean low-cost energy resources is critical for meeting the demands associated with the world's growing population.^{1,2} Hydrogen is expected to play an important role in fuel cells and therefore sustainable methods to obtain hydrogen are important. The hydrogen evolution reaction (HER) is one approach to produce hydrogen from water splitting and typically uses electrocatalysts such as Platinum (Pt) group metals. However, even though Pt based materials are the most effective electrocatalytic materials for a water splitting, they are expensive due to their limited supply and high demand.³⁻⁵ Therefore developing other non noble-metal based HER catalysts is essential for the long term future of the hydrogen based energy systems.^{3,6}

The HER performance of a catalyst is highly dependent upon its surface structure, with the optimal situation arising when the catalyst-hydrogen interaction is neither too strong nor too weak. ($\text{MH}_{\text{ads}}-\text{M}$ donates an empty metal active site and MH_{ads} represents an adsorbed H intermediate.) This results in a Gibbs free energy of adsorbed hydrogen close to zero (*e.g.* $\Delta G_{\text{H}}^0 \approx 0$ using H_2 as reference) for the catalytic surface. The volcano plot originally proposed by Parsons and Gerischer describes this scenario well, with the apex of the plot having the desirable behavior, such as Pt.^{7,8} Comparison of the exchange current densities of the common metals at their corresponding free energy of adsorbed H ΔG_{H}^0 importantly reveals the value of MoS_2 follows perfectly the same trend as those of Pt group metals, suggesting MoS_2 -based materials as promising alternative to noble metals for HER.

MoS_2 is in the group of transition metal dichalcogenides (TMDs, *i.e.*, MX_2 , where transition metal $\text{M} = \text{Mo}$ or W and chalcogen $\text{X} = \text{S}$, Se , or Te). It has a 2D layered structure with interlayer van der Waals (vdW) forces similar to graphite.^{7,9-19} A single MoS_2 layer has three atoms in thickness, with Mo in the middle and S atoms on top and below, where the Mo and S atoms are bonded by strong ionic-covalent

bonds.^{20, 21} The distance between a Mo atom and its nearest S atom is 2.41 Å. The thickness of each S-Mo-S layer is ~3.15 Å, while the distance between adjacent layers is ~3.49 Å, suggesting the interlayer vdW interaction is weaker than intra-layer covalent bonding.²²⁻²⁵

Improving HER catalyst performance involves many factors such as, increasing the density of active sites and the catalytic activity of individual active sites, as well as increasing the electron transfer and diffusion between a catalyst and its conductive substrate.^{11, 26} HER catalytic activity involves chemical interactions between adsorbed hydrogen and the dangling bond/unsaturated atom at edge sites of the catalyst along with changes in electronic structures adjacent to the edges.^{5, 27}

Nanostructured layered molybdenum disulfide (MoS_2) and its derivatives (molybdenum sulfides MoS_x) have been explored theoretically and experimentally in water splitting devices based on the catalytic properties towards HER.^{28, 29} MoS_2 has many other interesting properties,^{17, 18, 23, 30-32} which allow it to be used in the fields of lubrication,³³⁻⁴⁰ 2D transistor,^{13, 20, 25} hydrodesulphurization catalysis,^{2, 41-43} and energy storage.⁴⁴⁻⁴⁶ The edge site in MoS_2 monolayers has also been studied for catalytic activity in the HER,^{8, 47} Vertical alignment of MoS_2 in thin films has been shown to increase the density of active sites, leading to improved catalytic performance.^{7, 48, 49}

Edge-rich nanostructured MoS_2 catalysts have been synthesized by hydro-sulfurization of Mo coated substrates,¹⁰ thermal conversion,^{3, 33, 50} chemically exfoliation,⁵¹ chemical vapor deposition (CVD),^{4, 43, 44} and surfactant-assisted low-temperature solution processing.⁵² Dense vertically-aligned MoS_2 layers have been produced by sulfurizing elemental metal (Mo) seed layers,^{47, 48, 53} and vapor sulfurization of sponge-like molybdenum oxide layers.⁵⁴ Vertically oriented nanoplatelets are favourable for constructing “superaerophobic” surface due to the reduced adhesion of as-formed gas bubbles on the electrode surface by an order of magnitude compared to its counterparts. This enables quick removal of small bubbles and provides a constant working area, resulting in an improved electrocatalytic performance.⁵⁵ A porous structure can also have importance in electrochemically catalytic water splitting applications. Self-assembled porous MoS_2 thin films show high real surface area and a 3D open framework that enable efficient mass transport,⁵⁴ for example, H^+ and H_2 in the case of HER, through the high-surface area thin-film structure.⁴⁹ Developing high-porosity MoS_2 thin films utilizing a novel edge-exposed nano-platelet network with superaerophobic surface is expected to lead to high-performance HER electro-catalysts, but further work is needed to produce these structures using simple single step chemical synthetic methods.

Chemical vapor deposition (CVD) has been one of the most promising methods to grow wafer-scale and high-quality MoS₂ thin films on various substrates such as silicon oxide, sapphire, and graphite.^{16, 42}

Here we explore a scalable single-step chemical vapor deposition growth approach to produce edge rich MoS₂ nanoplatelet thin films with a high porosity network on a wide range of substrates including silicon wafers (SiO₂/Si-Si with 285 nm of SiO₂), glassy carbon, graphite and single wall nanotubes. The supported MoS₂ thin films can be easily integrated into different device architectures for electronic, optical sensing and, in the present case, electrochemical applications.⁴⁹ The growth of the nano-porous network is studied carefully to provide correlations between morphology, microstructure and electrochemical performance. Our results demonstrate the critical parameters that improve catalytic performance and can help guide the industrial optimization of MoS₂ electrocatalysts.

Results and Discussion

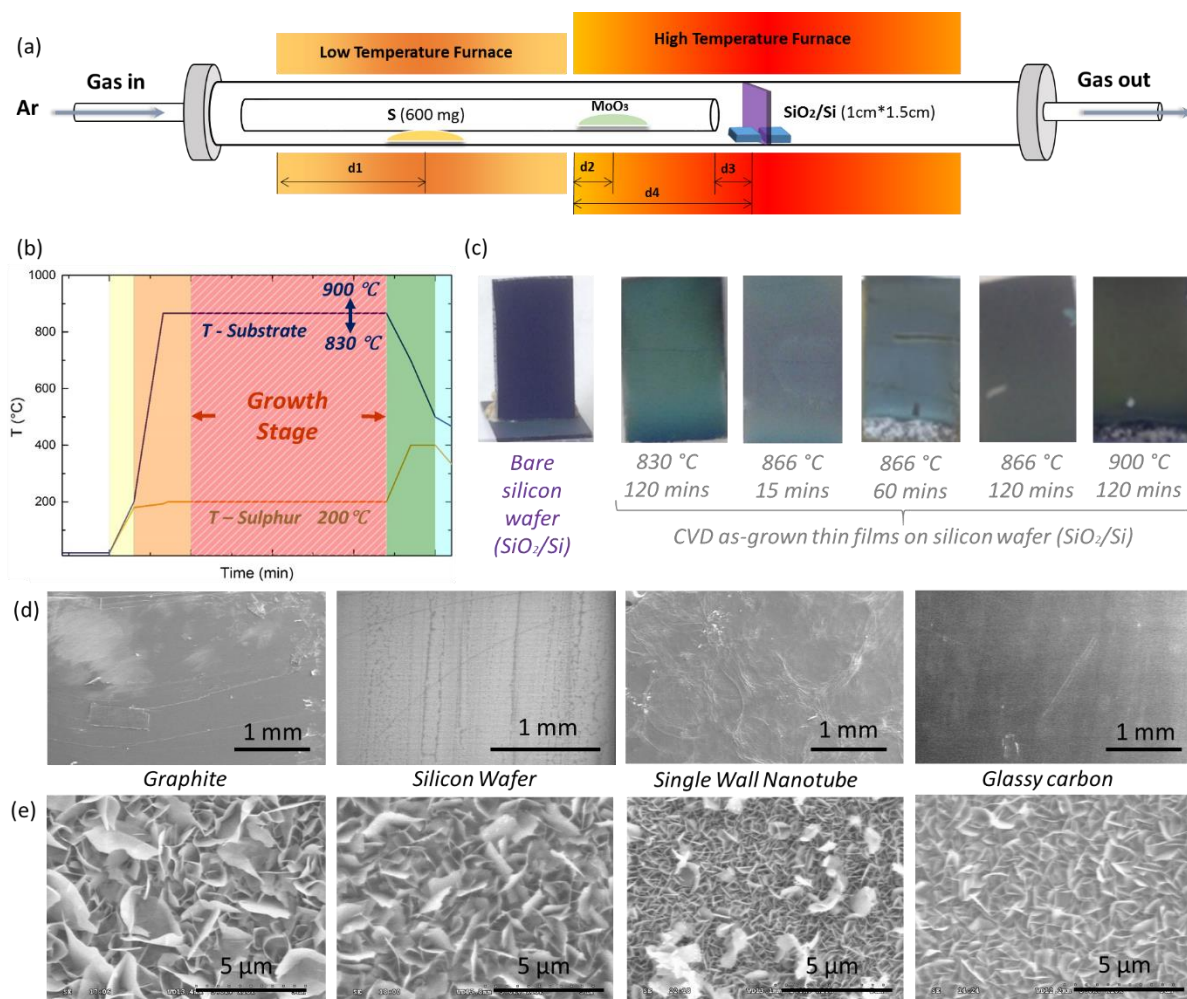


Figure 1. Atmospheric pressure CVD synthesis of edge-exposed MoS₂ nanoplatelet network on various substrates. (a) Schematic illustration of the CVD experimental set-up ($d_1 = 16$ cm, $d_2 = 2 \sim 3.5$ cm, $d_3 = 1$ cm and $d_4 = 15$ cm). (b) Temperature profiles of sulfur precursor and substrate programmed for the formation of edge-exposed MoS₂ thin film. (c) Optical image of vertically configured bare SiO₂/Si substrate and CVD as-grown edge-exposed MoS₂ thin films on SiO₂/Si substrate under growth temperature (temperature of substrate) of 830 °C, 866 °C and 900 °C; growth time of 15 mins, 60 mins and 120 mins, respectively. SEM images of graphite, silicon wafer (SiO₂/Si), single wall nanotube and glassy carbon substrates (d) before and (e) after deposition of edge-exposed MoS₂ thin films grown under the growth condition of 866 °C/60 mins with 50 s.c.c.m. of Ar gas.

The CVD synthesis of edge-exposed MoS₂ thin films on different substrates (silicon wafer, glassy carbon, graphite and single wall nanotube) is illustrated in Fig. 1a. A two-furnace approach is used in order to separately control the temperature of MoO₃ and S precursors (both are in powder form). 600 mg S powder was put upstream into an outer 1-inch quartz tube, right in the center of the low-temperature furnace; 500 ~ 1000 mg MoO₃ powder was scattered 2 ~ 3.5 cm off the start point of the high-temperature furnace. The double-quartz tube setup was applied to prevent quenching of MoO₃ from S. S and MoO₃ powders were heated to 200 °C and 300 °C ~ 400 °C in order to be evaporated; the vapor was carried downstream by argon gas onto the vertically configured substrate placed in the high temperature furnace, which eliminates the undesirable precursor mass depletion problem (*versus* notable concentration gradient of precursor vapor across substrate length in the case of substrate configured parallel to Ar gas flow) and neglects the diffusion and absorption process of reactants onto the substrate through the boundary layer of gas flow. The deposition temperature was set at 830 ~ 900 °C to for tunable morphology and microstructure of the as-deposited thin films.

Fig. 1b depicts the temperature profiles of S precursor and the substrate (as stated above MoO₃ powder was placed along with substrate on different site spots in the high temperature furnace, MoO₃ powder was heated and cooled simultaneously with the substrate) applied for the deposition of edge-exposed MoS₂ thin films. S powder was heated for 15 mins prior to introduction of MoO₃ vapor to ensure sufficient supply of S vapor in the reaction system. The above-mentioned CVD synthesis of desirable edge-exposed MoS₂ thin films was optimized by adjusting growth parameters such as carrier gas flow rate (10 s.c.c.m ~ 100 s.c.c.m of Ar gas), growth time (15 mins ~ 120 mins) and temperature (830 ~ 900 °C), mass amount (500 ~ 1000 mg) and positioning of MoO₃ (2 cm ~ 3.5 cm) as well as substrates (silicon wafer, glassy carbon, graphite and single wall nanotube). Optical images of a bare SiO₂/Si substrate and CVD grown

edge-exposed MoS₂ thin films on SiO₂/Si at different growth conditions (*i.e.* growth time and temperature) are shown in Fig. 1c, respectively. At higher deposition temperature and longer growth time, the as-deposited thin films are darker, which means more materials have been deposited onto the substrates. Fig. 1e presents scanning electron microscopy (SEM) images of as-grown thin films on different substrates (various bare substrates under SEM can be seen in Fig. 1d). The comparable platelet size (1 ~ 2 μm) and vertical alignment demonstrate the growth condition is transferrable, proving the generality of the growth process with respect to different substrates.

Flow rates from 10 s.c.c.m to 100 s.c.c.m of Ar gas were used for CVD synthesis of MoS₂ at 866 °C for 120 mins. The products were then examined under SEM as discussed in Fig. S1, demonstrating flow rate of carrier gas poses a remarkable effect on both material coverage and product morphology. Ar flow rate of 50 s.c.c.m is the optimum growth condition, a compromise between mass transport of precursor species and surface reaction, yielding dense array of edge-exposed MoS₂ nano platelets.

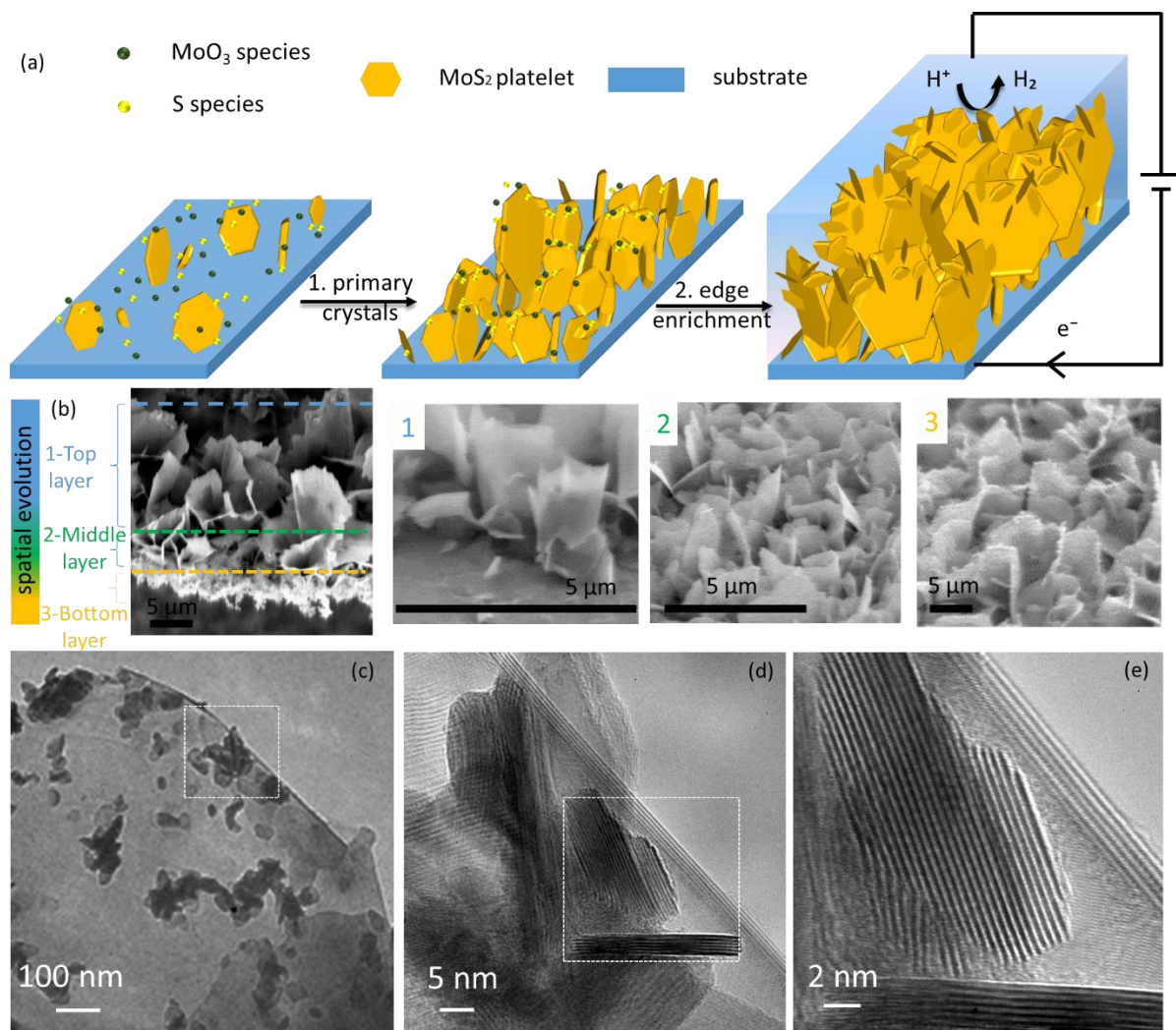


Figure 2. Configuration and Edge Enrichment mechanism for formation of vertically-aligned MoS₂ network. (a) Demonstration of Edge Enrichment mechanism, comprising (1) primary crystal formation and (2) edge enrichment process. (b) Spatial evolution of the as-grown MoS₂ thin film in the direction perpendicular to substrate surface, consisting of three layers in the aspects of different platelet size during growth (as indicated by dashed lines). (c to e) Low to high magnification TEM images of the petal site from top-layer crystals, on which vertically-aligned nanoflakes are nucleated. (Sample grown at 866 °C under 50 s.c.c.m of Ar gas for 120 mins with positioning of MoO₃ at 3.3 cm)

In order to understand the formation and growth mechanism of CVD-synthesized MoS₂ nanoplatelets, the morphological evolution was investigated. The tilted SEM image of the sample grown at 866 °C with 50 s.c.c.m of Ar gas for 120 mins in Fig. 2b, shows the material consists of multi-layered nanoplatelets. The observation of nanoplatelets in the perpendicular direction to the substrate suggests that earlier-formed

layers of platelets with smaller average size are stacked underneath by the layers of larger nanoplatelets. The film can be roughly divided into three sections: a bottom layer of very fine crystals (average size, $< 0.5 \mu\text{m}$), a middle layer formed by slightly larger crystals (average size, $1 \sim 2 \mu\text{m}$) and a top layer of larger platelets with size of $\sim 5 \mu\text{m}$.

The time evolution in Fig. 3a reveals a growth mechanism that involves two steps: (1) formation of primary crystals and (2) growth of secondary crystals off the primary ones. Growth starts with primary nucleation and growth of MoS_2 on the bare substrate till the substrate surface is fully occupied with a layer of MoS_2 fine crystals. These primary-grown crystals then serve as sites for crystallization of the MoS_2 to form new smaller domains with perpendicular orientation. This growth mechanism is supported by the TEM images in Fig. 2c-e showing abundant vertically orientated layers, which makes the structure promising for catalytic applications by providing a large number of edge sites. Further support of the proposed growth model can be found in Fig. S2-3.

Samples synthesized with different growth times had variations in the average growth rate, as shown in Fig. 4a, likely from the discrepancy posed by the different supports. The initial nucleation occurs at the beginning of the deposition process when primary MoS_2 molecules nucleate on the bare substrate, whereas secondary nucleation occurs on the primary MoS_2 crystals themselves once they cover the substrate surface and the different surface chemistry will lead to different growth rates. Therefore, the shorter growth time, corresponding mainly to primary nucleation and crystal growth, results in slower average film growth. The longer growth time, involving secondary nucleation and growth, leads to much faster film growth. This edge enrichment mechanism also facilitates a continuous pathway for electron transfer within the film, which is beneficial for catalytic activity with lowered resistivity.

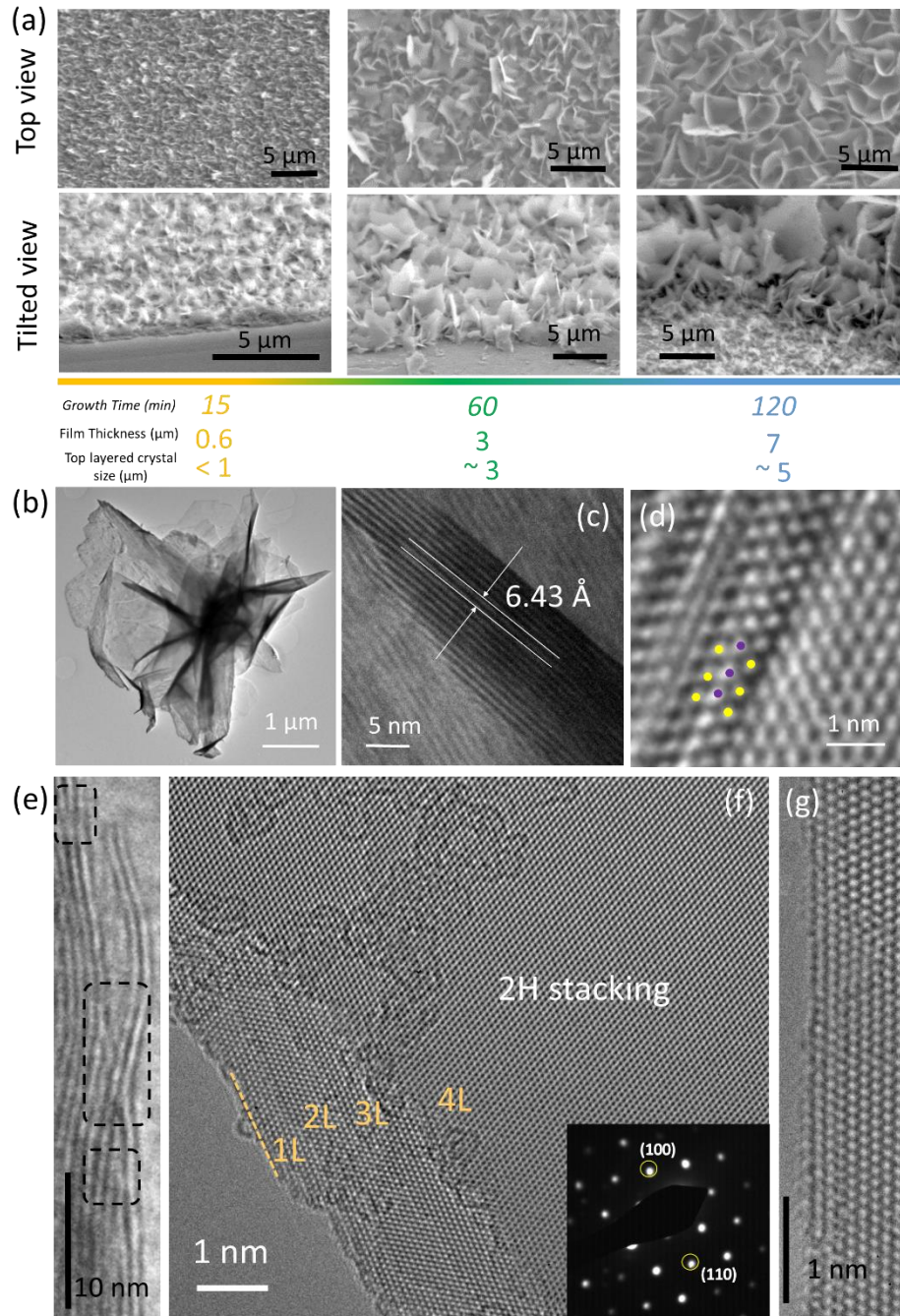


Figure 3. Time evolution and atomic structure of an edge enriched MoS₂ thin film. (a) SEM images depicting morphology (shown by zero tilt SEM images) and film thickness (shown by 60° tilt SEM images) evolution of the as-deposited nano-platelet thin films at 866 °C with 50 s.c.c.m of Ar gas as a function of time: 15 mins, 60 mins and 120 mins, respectively. TEM images of 120-min MoS₂ thin film: (b) nanosheet cluster from top layer; (c) perfectly vertically aligned platelet consisting of few layers with inter-layer spacing (d_{001}) of 6.43 Å; (d) atom

resolved vertically standing S-Mo-S layer; (e) a dislocation-rich vertical-standing nanoplatelet and (f) atomic structure of MoS₂ few layers with (g) smooth zigzag edge, inset: diffraction pattern.

The morphology and film thickness change with growth time, as shown in top and tilted SEM images (Fig. 3a) of samples synthesized for different time. In general, longer growth time leads to thicker as-grown films and larger top layered crystals. At an early stage - growth time of 15 mins, fine nanoplatelets are crystallized on the substrate, delivering a film thickness of less than 1 μm (#), and a growth time of 60 mins leads to a 3 μm thick film with the earlier-formed layer # maintained and a new layer of larger crystals (*) stacked on top. When increasing the growth time to 120 mins, the film is even thicker ($\sim 7 \mu\text{m}$), with layers # and * underneath, another new top layer of even larger crystals are grown on top of the former two. Film thickness determination is discussed in Fig. S4.

The as-grown thin films consisting of layers of nanoplatelets are further examined by aberration corrected TEM (AC-TEM) images. Fig. 3b shows a typical bundle of platelets from top layer of the film, the size of which is consistent with what is measured from low magnification SEM images (average size, 2 ~ 4 μm). Vertically standing layers with interlayer spacing of 6.43 Å are recorded as in Fig. 3c and atomic configuration S-Mo-S is resolved in Fig. 3d. The vertically standing nanoplatelet structure can have edge dislocations present, as shown in Fig. 3e, which is beneficial for HER activity. Fig. 3f shows the lattice structure of horizontally orientated 4-layer (4L) MoS₂ with good crystallinity and 2H stacking order. The atomic resolved AC-TEM imaging of the edges of the MoS₂ nanoplatelets shows they have dominant zigzag termination that is relatively clean and smooth, as shown in Fig. 3g. Selected area electron diffraction (SAED) patterns were recorded from the flat regions of the horizontally aligned MoS₂ and confirmed the single crystal layered structure with 2H stacking. As discussed above, the edge-rich features revealed in the AC-TEM images share consistency for all the samples in the present study as seen in detail in Fig. S5.

The two factors to improve HER performance of a catalyst: number of surface active sites (grain size) and reaction kinetics (charge transfer and diffusion within the film controlled by film thickness; contact between catalyst and substrate) are coupled due to the multi-stack growth nature of this particular high-porosity network. In order to optimize the device-oriented HER activity, the two areas should be improved at the same time; or one enhanced without sacrificing too much of the other, which can be tuned by growth time, precursor quantity and temperature.

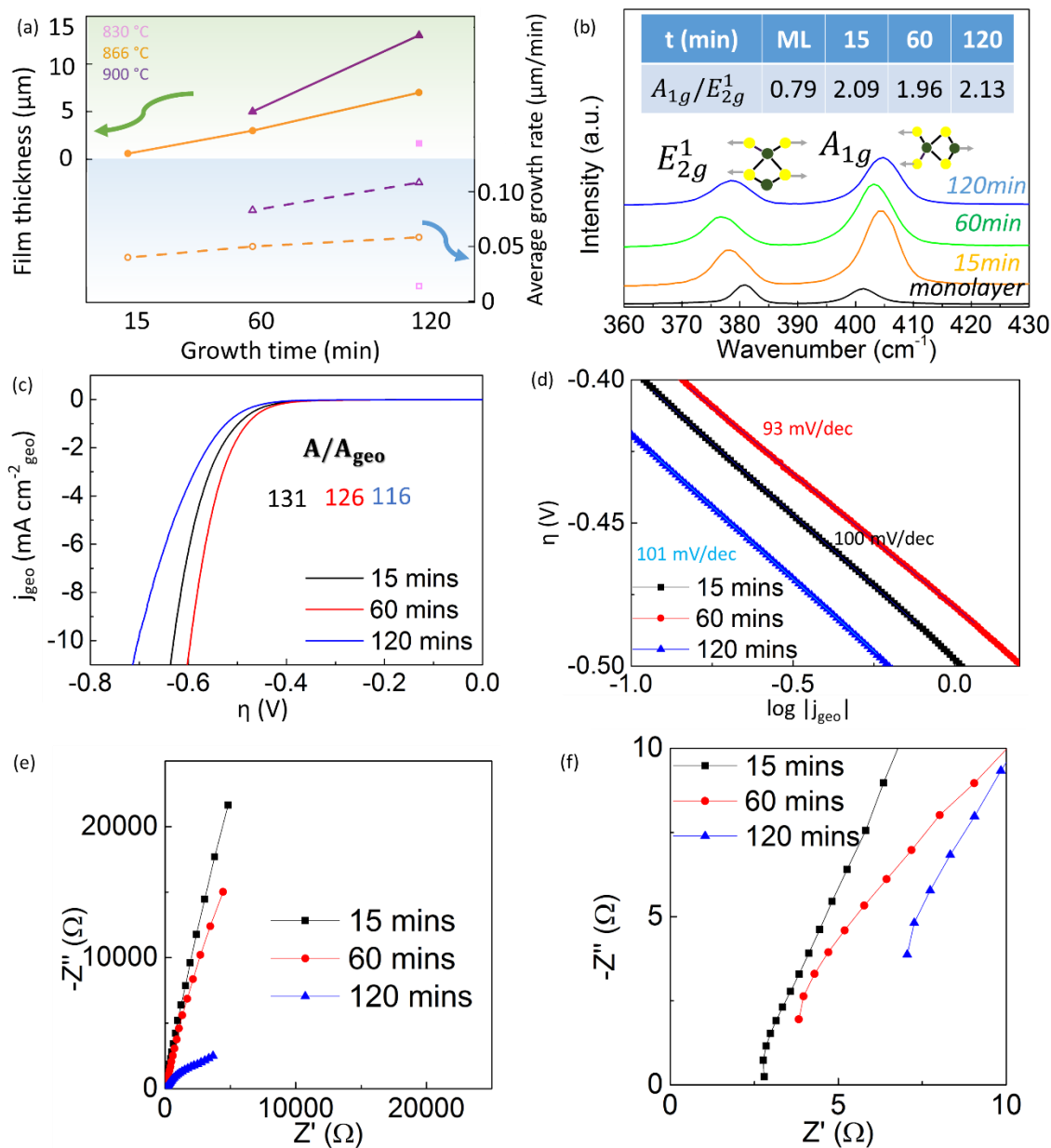


Figure 4. (a) Dependence of CVD film thickness and average growth rate on growth time (15 mins, 60 mins and 120 mins) and temperature (830 °C, 866 °C and 900 °C). (b) Raman spectra of MoS₂ samples grown for 15 mins, 60 mins, 120 mins, respectively. The spectrum for MoS₂ monolayer is obtained from a sample grown using methods reported in reference.⁴² Inset: schematics of two characteristic Raman vibration modes in MoS₂: in-plane vibration of molybdenum and sulfur atoms E_{2g}^1 and out-of-plane vibration of sulfur atoms A_{1g} ; information on peak intensity ratio of A_{1g}/E_{2g}^1 of samples synthesized for different growth time. (c) Cathodic polarization curves at scan rate of 1 mV/s with corresponding (d) Tafel plots and (e and f) electrochemical impedance spectroscopy (EIS) of CVD-

grown MoS₂ film on glassy carbon (values normalized by geometric area; A_{geo}: geometric area of the substrate; A: real surface area of the substrate).

Raman spectroscopy was used to confirm the CVD edge-exposed nanoplatelet thin films synthesized by aforementioned growth conditions are MoS₂. As seen in Fig. 4b, two characteristic peaks are revealed, corresponding to the two vibration modes for MoS₂: in-plane vibration of molybdenum and sulfur atoms E_{2g}¹ and out-of-plane vibration of sulfur atoms A_{1g}, respectively. The result is consistent with what has been commonly reported in the literature for bulk MoS₂ materials.^{56, 57} Here, the spectrum of a MoS₂ monolayer grown using different synthesis conditions as previously reported is presented as a reference.⁴² Compared to monolayer MoS₂, all the samples studied in the present work show a trend of decreased frequency of E_{2g}¹ and increased frequency of A_{1g}, which is due to increased thickness (layer numbers) based on the model of van der Waals interaction and long-range coulombic interaction,⁵⁶ respectively. Apart from positions of these two characteristic peaks, E_{2g}¹ and A_{1g}, the intensity ratio A_{1g}/E_{2g}¹ also provides information on the texture of as-grown MoS₂ thin films due to the fact that E_{2g}¹ corresponding to in-plane Mo-S phonon is preferentially excited for terrace-oriented thin films, whereas A_{1g} corresponding to out-of-plane Mo-S phonon is preferential for edge-oriented thin films.⁴⁷ As depicted in the inset table of Fig. 4b, the intensity ratio A_{1g}/E_{2g}¹ increases significantly from 0.79 of the terrace surface from monolayer MoS₂ to ~ 2, clearly indicating increased vertical orientation of the CVD grown thin films, matching well with the observations from SEM images.

HER electrocatalytic performance of CVD-grown high-porosity network of edge enhanced MoS₂ nanoplatelets were investigated by linear sweep voltammetry (LSV). The HER for water splitting generally involves three basic steps:¹¹ 1) adsorption of H⁺ on the catalyst active sites (Volmer step), 2) the formation of an intermediate H_{ad} (Tafel step) and 3) the desorption of hydrogen from the active sites (Heyrovsky step).⁵⁸ In acidic solutions, the three reaction steps have been proposed for the conversion of H⁺ to H₂. Tafel slopes of 120, 40 and 30 mV/dec are referred as the Volmer, Heyrovsky, and Tafel steps, respectively which suggests the rate-determining step in the HER mechanism. MoS₂ catalysts were deposited by the aforementioned CVD method directly onto 3 mm thick glassy carbon plates, which are used as the working electrode in a typical three-electrode electrochemical cell with 0.5 M H₂SO₄ solution. The cathodic polarization curves at the scan rate of 1 mV/s were recorded and shown in Fig. 4c. Tafel plots are shown in Fig. 4d. Exchange current density was determined, by fitting the linear portion of the Tafel plot at low cathodic current to the Tafel equation ($\eta = b \log|j| + a$, where j is the current density and

b is the Tafel slope).^{43, 47} Electrochemical impedance spectroscopy (EIS) was performed to investigate the electrode kinetics and interface reactions during HER process and shown in Fig. 4e and f.

In order to measure the real surface area of the thin films, the following method⁵⁹ has been used based on Cottrell's equation as discussed as following. Given homogeneous current distribution, the current, which is associated with the diffusion controlled charge transfer to a reactant, is written by $i = nFADc/\delta$, where D is the diffusion coefficient, c the bulk concentration and δ the thickness of the diffusion layer. Under the proviso that $c = c$ at $t = 0$ and $c = 0$ at the electrode surface at $t > 0$, δ at time t is given by $\delta = \sqrt{(\pi Dt)}$. Then by potentiostatically recording the current as a function of time: $A = i/nFc/\sqrt{(D/\pi t)}$, the surface area of the catalyst can be determined via the reaction of $K_3Fe(CN)_6 \rightarrow K_4Fe(CN)_6$. The surface area of all the tested samples is summarized in Table S2, with their geometrical area of either 0.8 or 0.52 cm².

As the growth time increases, the grain size of MoS₂ nanoplatelets also increases and measurements of the real surface area show a concomitant reduction (i.e A/A_{geo} decreased from 131 to 116, see Figure 4c). This is attributed to a reduced density of edges with larger platelet size. With increasing growth time the impedance of the catalyst film decreased in Fig. 4e and f, which gives improved electrode reaction kinetics. Comparison of corresponding polarization curves of 15mins, 60mins and 120mins growth times for MoS₂ (Fig. 4c) reveals three samples exhibit similar Tafel slopes of ~ 100 mV/dec (Fig. 4d), with the sample grown for 60 min performing the best in terms of cathodic current density, which is related to the production of hydrogen and is likely a compromise between accessible active sites and efficient electron transport.

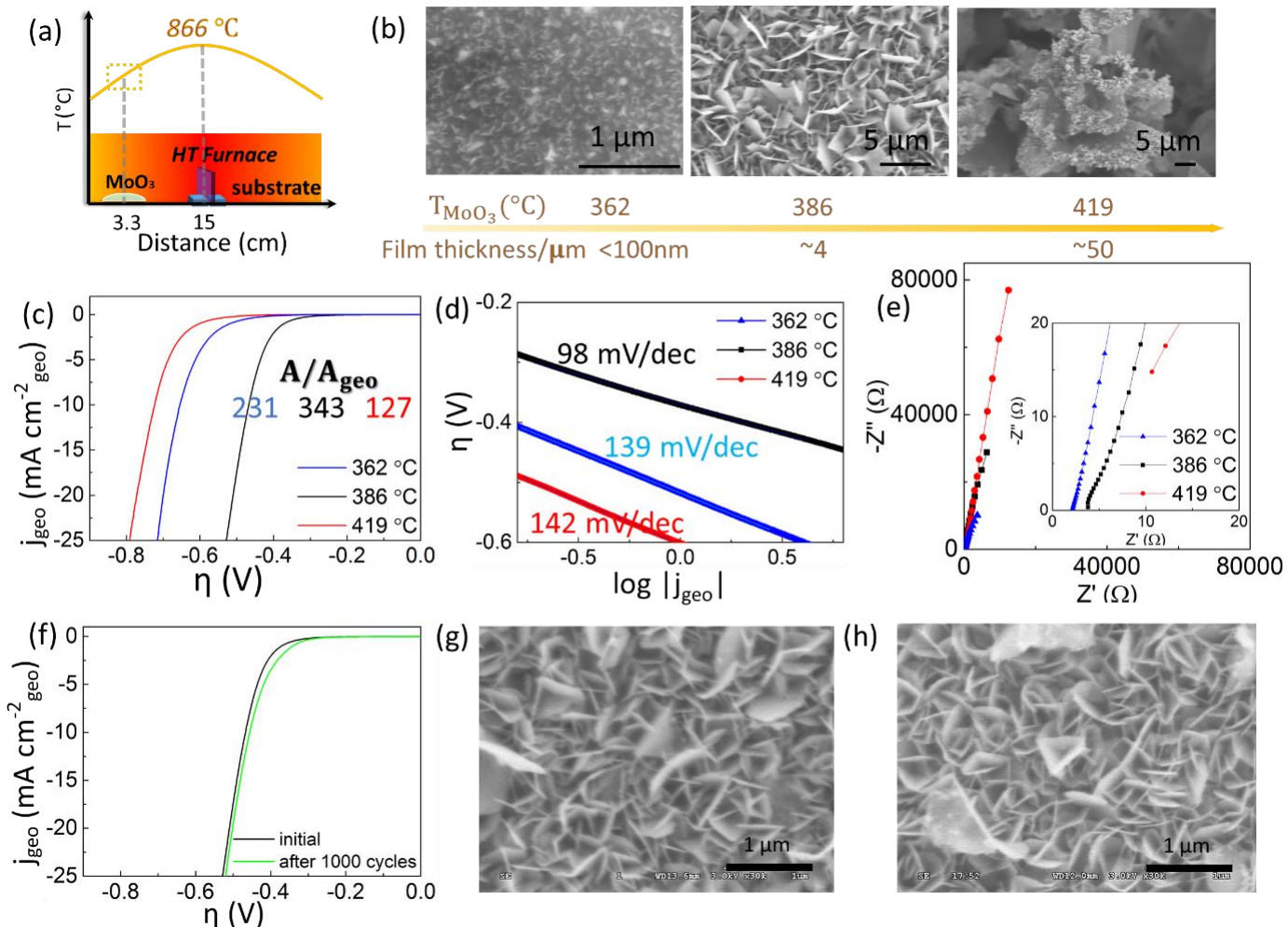


Figure 5. Influence of MoO_3 evaporation temperature on morphology and HER activity of MoS_2 thin films at 50 s.c.c.m of Ar gas for 120 mins. (a) Schematic illustration of temperature profile for the high temperature furnace chamber with set temperatures at 866 °C. (b) SEM images of the as-deposited thin films with MoO_3 positioning at 362 °C, 386 °C and 419 °C. (c) Cathodic polarization curves at scan rate of 1 mV/s with (d) corresponding Tafel plots and (e) EIS of CVD-grown edge-rich MoS_2 film on glassy carbon (values normalized by geometric area; A_{geo} : geometric area of the substrate; A : real surface area of the substrate). Electrochemical stability test of the optimum CVD-synthesized edge-exposed MoS_2 thin film on glassy carbon: (f) polarization curves and SEM images of the catalyst (g) before and (h) after 1,000 cycles, respectively.

To increase the density of catalytic active sites, more material can be deposited per geometric area (i.e area of substrate) while preserving the edge rich structure. Change the mass amount of precursor used for growth is considered effective to increase the evaporation rate, which will be reflected in the concentration of precursor in the vapor phase and thus the quantity of product. As shown in Fig. S7, impedance Z' values

corresponding to 500 mg, 800 mg and 1000 mg MoO_3 are $\sim 3 \text{ k}\Omega$, $\sim 88 \text{ k}\Omega$ and $\sim 300 \text{ k}\Omega$, which is in accord with the film thicknesses of $\sim 10 \text{ }\mu\text{m}$, $\sim 50 \text{ }\mu\text{m}$ and $\sim 100 \text{ }\mu\text{m}$. 500 mg of MoO_3 for CVD-growth is more favorable to deliver a higher performed catalytic water splitting device by providing adequate electrical conductivity.

Apart from direct adjustment of MoO_3 amount, control of MoO_3 evaporation temperature and growth temperature also enable product morphology tunable for optimum catalytic activity towards water splitting. According to the temperature profile of the reaction chamber as depicted in Fig. 5a (actual temperature of high-temperature furnace at different set values can be seen in Fig. S8), the actual temperature that MoO_3 undergoes can be controlled by adjusting the positioning of the MoO_3 powders. A set of experiments with positioning MoO_3 powder at $362 \text{ }^\circ\text{C}$, $386 \text{ }^\circ\text{C}$ and $419 \text{ }^\circ\text{C}$ (distance off the left start point of high temperature furnace) were conducted, with the other experimental parameters remaining constant. The SEM images (Fig. 5b) of the thin films show clearly: when MoO_3 powder moves closer to the furnace center (leading to higher evaporation temperature), the nanoplatelet morphology is retained with larger crystals (average size from $<100 \text{ nm}$ to $\sim 4 \text{ }\mu\text{m}$ and then to $\sim 20 \text{ }\mu\text{m}$) and film thickness (from $<100 \text{ nm}$ to $\sim 4 \text{ }\mu\text{m}$ and then to $\sim 50 \text{ }\mu\text{m}$).

Three samples with MoO_3 powder set at $362 \text{ }^\circ\text{C}$, $386 \text{ }^\circ\text{C}$ and $419 \text{ }^\circ\text{C}$ during CVD growth were tested for hydrogen generation performance. From Fig. 5c, it can be seen that $386 \text{ }^\circ\text{C}$ MoS_2 performs best among the three in terms of cathodic current density. In accordance with the SEM results, low precursor temperature leads to insufficient evaporation of reactant species in the vapor phase and reaction rate and thus reduced the material coverage on the substrate ($A/A_{\text{geo}} = 231$). When the temperature was too high, the excessive precursor flux to the sample results in increased grain size, which will in turn decreases the total number of accessible active edge sites participating in the HER reaction ($A/A_{\text{geo}} = 127$). On the other hand, higher precursor temperature delivers a thicker film with higher impedance, (Fig. 5e). So, an intermediate temperature (in this case, $386 \text{ }^\circ\text{C}$) is optimal for the growth of the MoS_2 HER catalyst to maximize real surface area ($A/A_{\text{geo}} = 343$) of the film without sacrificing charge transfer to the electrode.

The optimum $386 \text{ }^\circ\text{C}$ grown MoS_2 exhibits excellent hydrogen production activity ($60 \text{ mA/cm}_{\text{geo}}^2$ at an over-potential of 0.64 V vs. RHE) and exchange current density ($23 \text{ }\mu\text{A/cm}_{\text{geo}}^2$) for given geometric area. The exchange current density is amongst the highest values reported for MoS_2 catalysts ($0.25 \sim 18.2 \text{ }\mu\text{A/cm}^2$).^{3, Error! Bookmark not defined., 60-62} A Tafel slope of 98 mV/dec lies in the lower side of the range: $40 \sim$

212 mV/dec,^{2, 3, 7, 47, 53} which indicates the rate determining step of the HER is the Volmer reaction, a process to convert protons to adsorbed atoms on the highly-porous MoS₂ surface. Summary of HER activity performances of literature and present pure MoS₂ catalysts are recorded in Table S4. When normalized by the real surface area, the exchange current density (1.58 $\mu\text{A}/\text{cm}^2$, see details in Fig. S9-10) is not as superior as that over the geometric area. Further attempts for improving intrinsic activity could potentially be by doping and intercalation. Combined with the high surface area structure, the HER performance can be largely enhanced. The influence of synthesis temperature on surface morphology, film thickness and HER activity follows a similar trend as the growth temperature (Fig. S11-12).

The real and geometric surface areas of all samples tested for electrochemical performance towards HER are examined in Table S2. It is found that the edge-exposed nano-platelet network has a high real surface area to geometric area ratio (A/A_{geo}) up to 343. The relatively low Tafel slope and high exchange current density of present catalyst suggests the high-efficiency of such designed morphology and structure.

Long term durability testing is also an important concern for electrocatalysts, which demonstrates its thermodynamic stability. The optimum 386 °C grown MoS₂ catalyst was subjected to cycling-treatment in an acidic environment using cyclic voltammetry with a fast scan rate of 100 mV/s in order to simulate the practical working conditions of water splitting devices. The polarization curves and SEM images before and after the cycling treatment were recorded in Fig. 5f-h. Negligible change of the cathodic current and surface morphology was observed, which indicate durability of the as-grown catalyst.

Conclusion

We have directly engineered an edge-rich MoS₂ thin film by CVD, which has high porosity and large real surface area. This is achieved by controlling the growth conditions to promote a secondary growth stage that allows smaller MoS₂ flakes to grow perpendicular from the main preexisting flakes attached to the substrate and leads to an increase in the total number of edge sites. By systematically controlling the growth condition, tunable film thickness and surface morphology were achieved, enabling optimized combination of active site quantity, inter-planar charge transport and sufficient binding with the substrate as well as fast removal of gas bubbles via a superaerophobic surface. The observed HER catalytic performance over a given geometric area with long term durability is amongst the best reported to date. The moderate HER activity per real surface area is compensated by the vastly enhanced high surface area

porous structure. Further attempts could be made to improve the intrinsic catalyst activity of MoS₂ by doping and intercalation.

Experimental

Synthesis. The edge-exposed MoS₂ thin film was synthesized by chemical vapor deposition (CVD) method as illustrated in Fig. 1. Various precursor masses, substrates, reaction times, growth temperatures and carrier gas flow rates for CVD synthesis were investigated in order to obtain the optimum edge-terminated surface structure. Two-furnace double-quartz tube system was applied to control the temperature of MoO₃ and S separately. Growth was carried out on different substrates: silicon wafer (SiO₂/Si-Si with 285 nm of SiO₂), glassy carbon, graphite and single wall nanotube. After cleaning with acetone, substrates were then placed vertically into the center of inner quartz tube. 500 ~ 1000 mg of molybdenum (VI) oxide (MoO₃) powder ($\geq 99.5\%$ Sigma-Aldrich) powder was scattered 2 ~ 3.5 cm off the start point of the high-temperature zone; 600 mg sulfur powder ($\geq 99.5\%$, Sigma-Aldrich) was put upstream in the outer 1-inch quartz tube, right in the center of the low-temperature zone. Argon was used to protect the system from oxygen and carry sulfur vapor from the upstream of the low-temperature tube for reaction. The CVD system was first flushed with 500 s.c.c.m. of Ar gas for 30 mins, with both furnaces kept at room temperature. Then the flow rate was adjusted to 150 s.c.c.m. of Ar gas, while the low-temperature furnace was heated up at first 15 °C/min to 180 °C then 1 °C/min to 200 °C; the high-temperature furnace to 830 ~ 900 °C at 40 °C/min, dwell after reaching set temperature, the total duration is 50 mins. Afterwards the flow rate was set 50 s.c.c.m. of Ar gas at growth temperature at 830 ~ 900 °C for 15 ~ 120 mins. After growth the residue sulfur power was flushed with 500 s.c.c.m of Ar gas for 15 mins by setting the low-temperature furnace at 420 °C (40 °C/min) while the temperature of high-temperature furnace remained at 700 °C, followed by fast cooling of the system with 500 s.c.c.m of Ar gas.

Characterization. Surface morphology and microstructure were analyzed by scanning electron microscopy (SEM) and (aberration-corrected) transmission electron microscope ((AC-)TEM) techniques, respectively. SEM characterization was carried out on Hitachi S-4300 with an accelerating voltage of 3.0 kV. TEM samples were prepared by gently rubbing the TEM grid across the face of the MoS₂ thin film to detach flakes and promote their adhesion to the lacey carbon TEM grid. Low magnification TEM was performed using a JEOL JEM-2100 with an accelerating voltage of 200 kV and AC-TEM was performed

using Oxford's JEOL JEM-2200MCO FEGTEM with a CEOS image corrector and operated at an accelerating voltage of 80 kV. Raman spectroscopy was measured using a JY Horiba Labram Aramis imaging con-focal Raman microscope with excitation wavelength of 532 nm.

Electrochemical studies. Electrochemical testing was performed in 0.5 M H₂SO₄ Ar-purged solution using a three-electrode setup for measurement of electrocatalytic activities towards HER, with Ag/AgCl/KCl (3M) as reference electrode ($E(\text{RHE}) = E(\text{Ag/AgCl} / \text{KCl (3M)}) + 0.21 - 0.059 \cdot \text{pH}$), and an activated carbon counter electrode. A 3 mm thick glassy carbon plate (Sigma-Aldrich Company Ltd.) containing the CVD grown edge-exposed MoS₂ films was used as the working electrode. The effective area (1 cm × 0.8 cm) of the working electrode was defined by applying electrochemically inert hydrophobic wax and pure polytetrafluoroethylene (PTFE) tape. A metal clip was used to connect the working electrode with an external circuit. Linear sweep voltammetry (*abbrev.* LSV, scan rate of 1 mV/s) under quasi-equilibrium conditions were recorded by a Biologic VMP3 potentiostat. Cyclic voltammetry (*abbrev.* CV) was conducted at 100 mV/s to investigate the cycling stability. The Electrochemical Impedance Spectroscopy (*abbrev.* EIS) was carried out from 200000 to 1 Hz with an amplitude of 10 mV.

Supporting Information. Fig. S1: Influence of carrier gas flow rate on CVD growth of MoS₂; Fig. S2-3: SEM images for verification of edge enrichment mechanism; Fig. S4: Measurement method of film thickness; Fig. S5a-h: TEM images and diffraction patterns of all the thin films in the present study; Fig. S6-7: Influence of mass amount of precursor MoO₃ on surface morphology and HER activity of the as-deposited MoS₂ thin films; Fig. S8: Temperature gradient of high-temperature furnace at different set values; Fig. S9: Comparison of cathodic polarization curves of 386 °C MoS₂ normalized by geometric and real surface area; Fig. S10: Tafel plot of 386 °C MoS₂, normalized by real surface area; Fig. S11-12: Influence of synthesis temperature on surface morphology and HER activity of the as-deposited MoS₂ thin films; Table S1: Sample list in this work; Table S2: The real surface area of edge-exposed MoS₂ thin films; Table S3: Electrochemical analysis of edge-exposed MoS₂ thin films; Table S4: Summary of catalytic parameters of pure MoS₂ catalysts in literature and this study; Fig. S13: EIS spectroscopy of MoS₂ thin film at different overpotentials.

Acknowledgement

JHW thanks the Royal Society for support. This work was conducted under the framework of the research and development program of the Korea Institute of Energy Research (B6-2452). SN acknowledges European Union's Horizon 2020 research and innovation programme under the Marie Skłodowska-Curie grant (659306).

References

- (1) Wu, Z.; Fang, B.; Bonakdarpour, A.; Sun, A.; Wilkinson, D. P.; Wang, D. *Appl. Catal., B: Environmental* **2012**, 125, 59-66.
- (2) Yan, Y.; Xia, B.; Ge, X.; Liu, Z.; Wang, J. Y.; Wang, X. *ACS. Appl. Mater. Interfaces* **2013**, 5, 12794-12798.
- (3) Yan, Y.; Xia, B.; Li, N.; Xu, Z.; Fisher, A.; Wang, X. *J. Mater. Chem. A* **2015**, 3, 131-135.
- (4) Zhou, G.; Xu, X.; Yu, J.; Feng, B.; Zhang, Y.; Hu, J.; Zhou, Y. *Cryst. Eng. Comm.* **2014**, 16, 9025-9032.
- (5) Xie, J.; Zhang, H.; Li, S.; Wang, R.; Sun, X.; Zhou, M.; Zhou, J.; Lou, X. W.; Xie, Y. *Adv. Mater.* **2013**, 25, 5807-5813.
- (6) Wang, H.; Tsai, C.; Kong, D.; Chan, K.; Abild-Pedersen, F.; Nørskov, J. K.; Cui, Y. *Nano Res.* **2014**, 8, 556-575.
- (7) Wang, H.; Zhang, Q.; Yao, H.; Liang, Z.; Lee, H. W.; Hsu, P. C.; Zheng, G.; Cui, Y. *Nano Lett.* **2014**, 14, 7138-7144.
- (8) Jaramillo, T. F.; Jorgensen, K. P.; Bonde, J.; Nielsen, J. H.; Horch, S.; Chorkendorff, I. *Science* **2007**, 317, 100-102.
- (9) Dai, Z. R.; Pan, Z. W.; Wang, L. Z. *Adv. Funct. Mater.* **2003**, 13, 9-24.
- (10) Gaur, A. P. S.; Sahoo, S.; Ahmadi, M.; Guinel, M. J. F.; Gupta, S. K.; Pandey, R.; Dey, S. K.; Katiyar, R. S. *J. Phys. Chem. C* **2013**, 117, 26262-26268.

- (11) Chung, D. Y.; Park, S. K.; Chung, Y. H.; Yu, S. H.; Lim, D. H.; Jung, N.; Ham, H. C.; Park, H. Y.; Piao, Y.; Yoo, S. J.; Sung, Y. E. *Nanoscale* **2014**, 6, 2131-2136.
- (12) Seh, Z. W.; Yu, J. H.; Li, W.; Hsu, P. C.; Wang, H.; Sun, Y.; Yao, H.; Zhang, Q.; Cui, Y. *Nat. Commun.* **2014**, 5, 5017.
- (13) Lee, Y. H.; Zhang, X. Q.; Zhang, W.; Chang, M. T.; Lin, C. T.; Chang, K. D.; Yu, Y. C.; Wang, J. T.; Chang, C. S.; Li, L. J.; Lin, T. W. *Adv. Mater.* **2012**, 24, 2320-2325.
- (14) Fu, X.; Qian, J.; Qiao, X.; Tan, P.; Peng, Z. *Opt. Lett.* **2014**, 39, 6450-6453.
- (15) Wang, H.; Liu, F.; Fu, W.; Fang, Z.; Zhou, W.; Liu, Z. *Nanoscale* **2014**, 6, 12250-12272.
- (16) Yu, Y.; Li, C.; Liu, Y.; Su, L.; Zhang, Y.; Cao, L. *Sci. Rep.* **2013**, 3, 1866.
- (17) Tan, L. K.; Liu, B.; Teng, J. H.; Guo, S.; Low, H. Y.; Loh, K. P. *Nanoscale* **2014**, 6, 10584-10588.
- (18) Sorkin, V.; Pan, H.; Shi, H.; Quek, S. Y.; Zhang, Y. W. *Crit. Rev. Solid State Mater. Sci.* **2014**, 39, 319-367.
- (19) Tran, P. D.; Pramana, S. S.; Kale, V. S.; Nguyen, M.; Chiam, S. Y.; Batabyal, S. K.; Wong, L. H.; Barber, J.; Loo, J. *Chemistry* **2012**, 18, 13994-13999.
- (20) Gong, Y.; Lin, J.; Wang, X.; Shi, G.; Lei, S.; Lin, Z.; Zou, X.; Ye, G.; Vajtai, R.; Yakobson, B. I.; Terrones, H.; Terrones, M.; Tay, B. K.; Lou, J.; Pantelides, S. T.; Liu, Z.; Zhou, W.; Ajayan, P. M. *Nat. Mater.* **2014**, 13, 1135-1142.
- (21) Wang, R.; Xu, C.; Sun, J.; Liu, Y.; Gao, L.; Yao, H.; Lin, C. *Nano Energy* **2014**, 8, 183-195.
- (22) Chen, D.; Chen, W.; Ma, L.; Ji, G.; Chang, K.; Lee, J. Y. *Mater. Today* **2014**, 17, 184-193.
- (23) Stephenson, T.; Li, Z.; Olsen, B.; Mitlin, D. *Energy Environ. Sci.* **2014**, 7, 209.
- (24) Park, K. T.; RichardsBabb, M.; Freund, M. S.; Weiss, J.; Klier, K. *J. Phys. Chem.* **1996**, 100, 10739-10745.

- (25) Radisavljevic, B.; Radenovic, A.; Brivio, J.; Giacometti, V.; Kis, A. *Nat. Nanotechnol.* **2011**, 6, 147-150.
- (26) Kim, J.; Byun, S.; Smith, A. J.; Yu, J.; Huang, J. *J. Phys. Chem. Lett.* **2013**, 4, 1227-1232.
- (27) Li, Y.; Wang, H.; Xie, L.; Liang, Y.; Hong, G.; Dai, H. *Journal. ACS* **2011**, 133, 7296-7299.
- (28) Feng, Q.; Duan, K.; Ye, X.; Lu, D.; Du, Y.; Wang, C. *Sens Actuators B Chem* **2014**, 192, 1-8.
- (29) Chianelli, R. R.; Siadati, M. H.; De la Rosa, M. P.; Berhault, G.; Wilcoxon, J. P.; Bearden, R.; Abrams, B. L. *Cat. Rev.* **2006**, 48, 1-41.
- (30) Benck, J. D.; Hellstern, T. R.; Kibsgaard, J.; Chakthranont, P.; Jaramillo, T. F. *ACS Catal.* **2014**, 4, 3957-3971.
- (31) Dong, L.; Lin, S.; Yang, L.; Zhang, J.; Yang, C.; Yang, D.; Lu, H. *Chem. Commun.* **2014**, 50, 15936-15939.
- (32) O'Neill, A.; Khan, U.; Coleman, J. N. *Chem. Mater* **2012**, 24, 2414-2421.
- (33) Vilas, G. P.; Swati, V. P.; Aharon, G. *Cryst. Growth Des.* **2008**, 8, 1126-1132.
- (34) Shaffer, S. J.; Rogers, M. J. *Wear* **2007**, 263, 1281-1290.
- (35) Lingertat, J.; Gradt, T.; Hathiramani, D.; Junghanns, P.; Laux, M.; Meine, K.; Schauer, F.; Schneider, T. *Fusion Eng. Des.* **2009**, 84, 1192-1196.
- (36) Holmberg, K.; Ronkainen, H.; Laukkanen, A.; Wallin, K.; Hogmark, S.; Jacobson, S.; Wiklund, U.; Souza, R. M.; Ståhle, P. *Wear* **2009**, 267, 2142-2156.
- (37) Bhaduri, D.; Kumar, R.; Jain, A. K.; Chattopadhyay, A. K. *Wear* **2010**, 268, 1053-1065.
- (38) Zabinski, J. S.; Bultman, J. E.; Sanders, J. H.; Hu, J. J. *Tribol Lett.* **2006**, 23, 155-163.
- (39) Onate, J. I.; Brizuela, M.; Viviente, J. L.; García-Luis, A.; Bracerias, I.; Gonzalez, D.; Garmendia, I. *Trans. IMF* **2007**, 85, 75-81.
- (40) Colas, G.; Saulot, A.; Godeau, C.; Michel, Y.; Berthier, Y. *Wear* **2013**, 305, 192-204.

- (41) Zhang, H.; Lin, H.; Zheng, Y.; Hu, Y.; MacLennan, A. *Appl. Catal., B* **2015**, 165, 537-546.
- (42) Wang, S.; Rong, Y.; Fan, Y.; Pacios, M.; Bhaskaran, H.; He, K.; Warner, J. H. *Chem. Mater* **2014**, 26, 6371-6379.
- (43) Zhu, H.; Du, M.; Zhang, M.; Zou, M.; Yang, T.; Fu, Y.; Yao, J. *J. Mater. Chem. A* **2014**, 2, 7680.
- (44) Prabakaran, A.; Dillon, F.; Melbourne, J.; Jones, L.; Nicholls, R. J.; Holdway, P.; Britton, J.; Koos, A. A.; Crossley, A.; Nellist, P. D.; Grobert, N. *Chem. Commun* **2014**, 50, 12360-12362.
- (45) Zhang, Q.; Yu, K.; Zhao, B.; Wang, Y.; Song, C.; Li, S.; Yin, H.; Zhang, Z.; Zhu, Z. *RSC Adv.* **2013**, 3, 10994.
- (46) Wang, J. Z.; Lu, L.; Lotya, M.; Coleman, J. N.; Chou, S. L.; Liu, H. K.; Minett, A. I.; Chen, J. *Adv. Energy Mater* **2013**, 3, 798-805.
- (47) Kong, D.; Wang, H.; Cha, J. J.; Pasta, M.; Koski, K. J.; Yao, J.; Cui, Y. *Nano Lett.* **2013**, 13, 1341-1347.
- (48) Jung, Y.; Shen, J.; Liu, Y.; Woods, J. M.; Sun, Y.; Cha, J. J. *Nano Lett.* **2014**, 14, 6842-6849.
- (49) Kibsgaard, J.; Chen, Z.; Reinecke, B. N.; Jaramillo, T. F. *Nat. Mater.* **2012**, 11, 963-969.
- (50) Li, P. G.; Lei, M.; Wang, X. F.; Tang, H. L.; Tang, W. H. *J. Alloys Compd.* **2009**, 474, 463-467.
- (51) Lukowski, M. A.; Daniel, A. S.; Meng, F.; Forticaux, A.; Li, L.; Jin, S. *J. ACS* **2013**, 135, 10274-10277.
- (52) Seo, J. W.; Jun, Y. W.; Park, S. W.; Nah, H.; Moon, T.; Park, B.; Kim, J. G.; Kim, Y. J.; Cheon, J. *Angew. Chem.* **2007**, 46, 8828-8831.
- (53) Wang, H.; Kong, D.; Johanes, P.; Cha, J. J.; Zheng, G.; Yan, K.; Liu, N.; Cui, Y. *Nano Lett.* **2013**, 13, 3426-3433.
- (54) Yang, Y.; Fei, H.; Ruan, G.; Xiang, C.; Tour, J. M. *Adv. Mater.* **2014**, 26, 8163-8168.

- (55) Lu, Z.; Zhu, W.; Yu, X.; Zhang, H.; Li, Y.; Sun, X.; Wang, X.; Wang, H.; Wang, J.; Luo, J.; Lei, X.; Jiang, L. *Adv. Mater.* **2014**, 26, 2683-2687.
- (56) Zhang, X.; Qiao, X. F.; Shi, W.; Wu, J. B.; Jiang, D. S.; Tan, P. H. *Chem. Soc. Rev* **2015**, 44, 2757-2785.
- (57) Li, H.; Zhang, Q.; Yap, C. C. R.; Tay, B. K.; Edwin, T. H. T.; Olivier, A.; Baillargeat, D. *Adv. Funct. Mater* **2012**, 22, 1385-1390.
- (58) Behranginia, A.; Asadi, M.; Liu, C.; Yasaei, P.; Kumar, B.; Phillips, P.; Foroozan, T.; Waranius, J. C.; Kim, K.; Abiade, J.; Klie, R. F.; Curtiss, L. A.; Salehi-Khojin, A. *Chem. Mater* **2016**, 28, 549-555.
- (59) Trasatti, S.; Petrii, O. A. *J. Electroanal. Chem.* **1992**, 327, 353-376
- (60) Zhang, K.; Zhao, Y.; Zhang, S.; Yu, H.; Chen, Y.; Gao, P.; Zhu, C. *J. Mater. Chem. A* **2014**, 2, 18715-18719.
- (61) Gao, M. R.; Chan, M. K.; Sun, Y. *Nat. Commun.* **2015**, 6, 7493.
- (62) Lu, Z.; Zhang, H.; Zhu, W.; Yu, X.; Kuang, Y.; Chang, Z.; Lei, X.; Sun, X. *Chem. Commun.* **2013**, 49, 7516-7518.